Messenger Neutron Spectrometer (NS) Calibration Report

David J. Lawrence, William C. Feldman, John Goldsten

Executive Summary

All of the required calibration measurements were completed for the Messenger NS. These include measurements of fast neutrons for eight different energies at the Columbia University Radiological Research Accelerator Facility (RARAF), thermal and epithermal neutrons at Los Alamos National Laboratory (LANL), and a broad energy range measurement of a ^{252}Cf neutron source at LANL. Preliminary analysis of the data have obtained the following results: 1) We have measured a fast neutron energy calibration that corresponds very favorably with a model for this type of scintillator that was calculated in 1994; 2) We have verified the expected angular dependence of the Li glass scintillators in response to thermal and epithermal neutrons; 3) We have determined the fast neutron efficiency of the BC454 plastic scintillator and it is within 20% of the modeled efficiency. It is also very similar to the efficiency measured for a similar sized sensor on Lunar Prospector.

Work left to do includes modeling the NS for both sets of calibration runs (i.e., at RARAF and LANL). These models will allow a more complete determination of the NS efficiency for all angles and energies. In addition, we will be completing desired high voltage and gain calibrations using gamma-ray sources on June 14 in Florida, where the NS is installed on the Messenger spacecraft. Based on our preliminary analyses of the data and a comparison of these data with other similar flight instruments, we conclude that the Messenger NS will meet or exceed all measurement requirements.

Messenger Neutron Spectrometer (NS) Calibration Report

David J. Lawrence, William C. Feldman, John Goldsten

1. Introduction

This document summarizes the calibration measurements and preliminary analyses that have been carried out for the Messenger Neutron Spectrometer.

2. Science Objectives and Instrument Description

The MESSENGER Neutron Spectrometer is part of the MESSENGER Gamma-Ray/Neutron Spectrometer (GRNS) instrument, and is known as GRNS/NS. The scientific objectives for GRNS/NS are:

1. To search for, and determine the abundance of water ice to depths of 100 cm within permanently shaded craters near Mercury's north pole.
2. To search for, and determine the abundance of hydrogen implanted by the solar wind into the Mercury regolith to depth of 100 cm near the northern cusps of the Mercury magnetosphere.
3. To map the average atomic weight of the Mercury soil.
4. Provide neutron flux correction measurements for use in the analysis of data from the gamma-ray spectrometer (GRNS/GRS).

The Messenger neutron spectrometer consists of a sandwich of three scintillators that are optically decoupled from each other. Each scintillator will be coupled independently to separate photomultiplier tubes (PMT). The first is a lithium glass scintillator (LG1) that is 4 mm thick by 10 cm x 10 cm in area. The second is a borated plastic (BP) scintillator (BC454 type scintillator) that is 10 cm thick by 10 cm x 10 cm in area. The third is a lithium glass scintillator (LG2) that is 4 mm thick by 10 cm x 10 cm in area. Figure 1 shows a diagram of the GRNS/NS. The two Li-glass scintillators respond to a combination of thermal and epithermal neutrons that span the range between 0 eV and about 1 keV. Discrimination between neutrons in the thermal ($E < 0.4$ eV) and low-energy part of the epithermal ($0.4 \text{ eV} < E < 1 \text{ keV}$) ranges, as well as neutrons coming from Mercury and those coming from the spacecraft, will be made by using the speed of the spacecraft relative to Mercury (~ 3 km/s at periherm). Another measure of the flux of epithermal neutrons ($0.4 \text{ eV} < E < 0.5 \text{ keV}$) is made by the singles counting rate of BP events that have a pulse-height that corresponds to the effective energy deposition value of the $^{10}B(n,\alpha)^{7}Li$ reaction. Time-correlated events in the BP provide a measure of the flux of fast neutrons ($0.5 \text{ MeV} < E < 7 \text{ MeV}$). These events are defined by a time-correlated pair of interactions in the BP scintillator. The first of these pairs corresponds to a neutron that loses all of its sensible energy in BP and the second interaction corresponds to the $^{10}B(n,\alpha)^{7}Li$ reaction. The signature of this type of event is an exponential time dependence (τ) of the time between first and second interactions (or Time To Second Pulse, TTSP) and a pulse-height of the second interaction that corresponds to the Q-value of the $^{10}B(n,\alpha)^{7}Li$ reaction. For BC454, $\tau = 2.2$ μs, and the equivalent electron energy of the recoil particles stemming from the nuclear reaction is $E_{ee} = 93$ keV. The pulse height of the first interaction then provides a measure of the energy spectrum of fast neutrons.

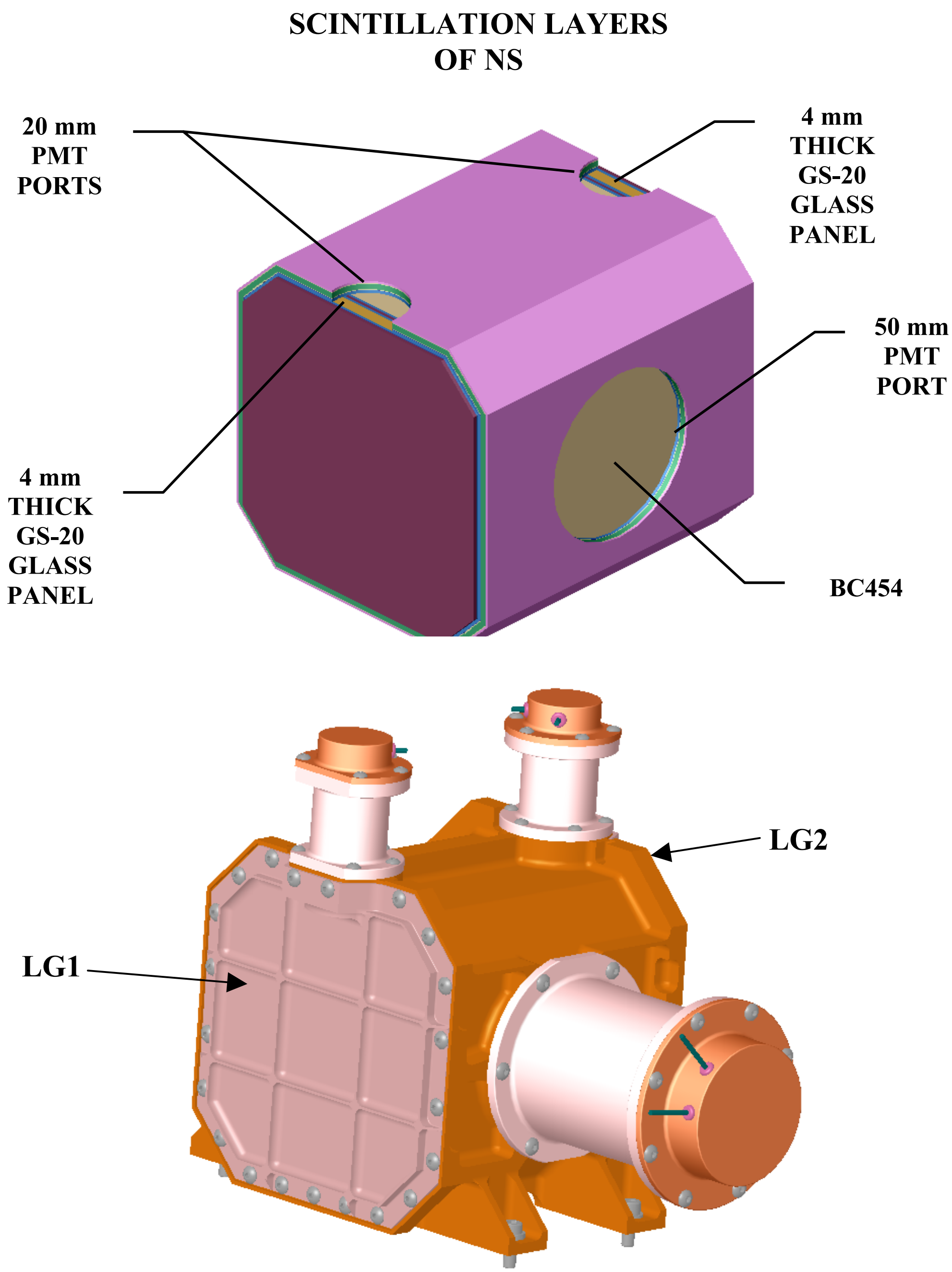

Figure 1. Two views of the GRNS/NS. The top shows the internal configuration of the three scintillators. The bottom shows the final external view.

To carry out the above science objectives, the GRNS/NS has the following measurement requirements:

1. Measure separately the flux of neutrons in the energy range between 0 eV and about 1 keV that are absorbed by the lithium glass (LiG or GS20) scintillator plates that face parallel and antiparallel to the spacecraft velocity vector when the Messenger spacecraft is in the dawn-dusk orbit about Mercury.
2. Measure the flux of epithermal neutrons in the energy range between about 0.4 eV and 500 keV that are absorbed by the borated plastic (BP, or BC454) scintillator.
3. Measure the flux of fast neutrons in the energy range between about 0.5 MeV and 7 MeV that deposit all of their energy in the BP scintillator.
4. Provide continuous in-flight gain calibration using the peak position of the $^{10}B(n,\alpha)^{7}Li$ reaction.
5. Measure all four ranges of neutron flux as a function of spacecraft altitude.
6. Measure LG spectra as a function of angle between the LG plate normals and the spacecraft velocity vector (to allow subtraction of spacecraft backgrounds).
7. Monitor the flux of high-energy protons and the flux of neutron beta-decay electrons (endpoint of 780 keV) using some of the energetic particle sensors aboard Messenger.

3.0 Pre-flight Ground Calibrations

3.1 Fast Neutron Calibrations

A set of calibration data was taken at the Columbia University Radiological Research Accelerator Facility (RARAF) using fast neutrons having energies from 0.5 – 14 MeV. This section describes the set up of the runs, a list of data that was taken, and preliminary results from the data.

3.1.1 NS Set up at RARAF

Figure 2 shows a schematic diagram of how the NS was set up at the RARAF location. The entire instrument was placed inside a small beam room, such that the surrounding concrete walls were located approximately 150 – 200 cm from the NS. Both the sensors and the flight electronics were attached to a metal plate that could be rotated in two dimensions. The azimuthally rotation, φ, is seen in Figure 2a and the polar rotation, θ, is seen in Figure 2b. Depending on the neutron energy, the NS was placed at different locations away from the beam target, as seen in Figure 2 and Table 1.

The entire set of runs were carried out with the flight electronics, which were connected to a Messenger GSE running GSEOS software.

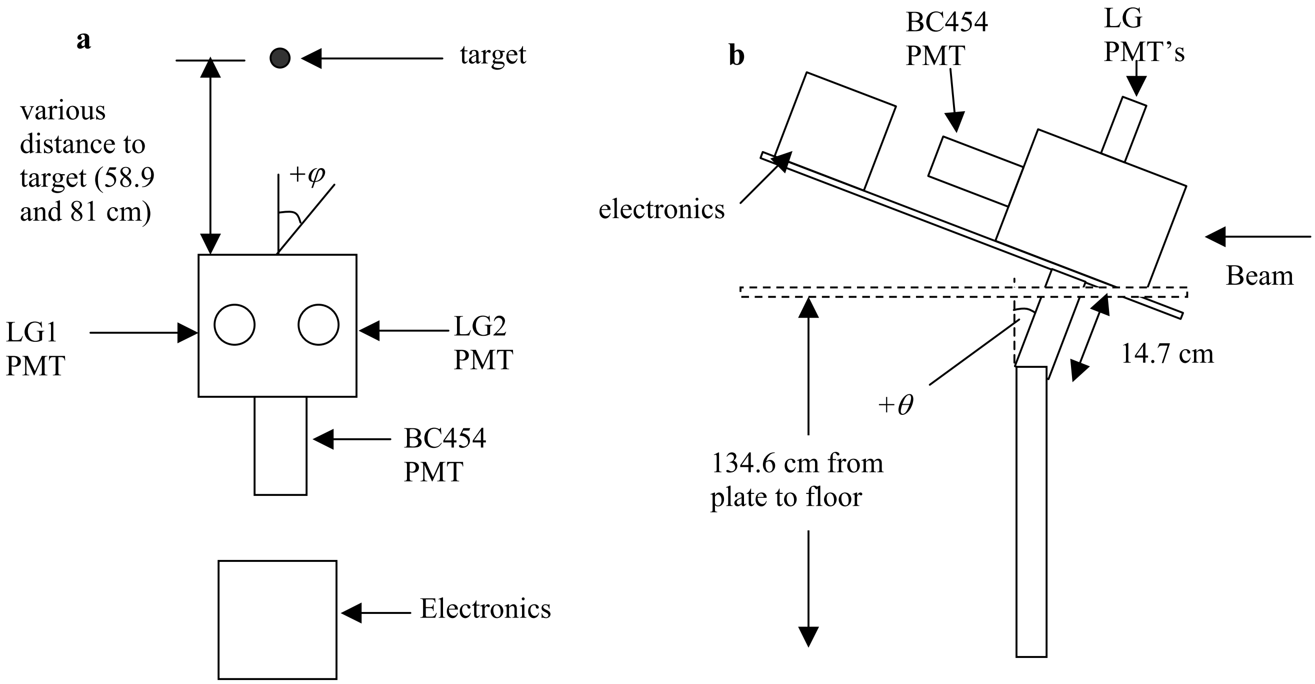

Figure 2: NS set up at RARAF. Figure 2a shows the NS from the top and Figure 2b shows the NS from the side.

3.1.2 List of Runs

Table 1 lists the different runs that were carried out at RARAF. The first column lists the run name, which is given by a date and time stamp. The second and third columns show the azimuthaly and polar angles given in degrees. The fourth column shows the neutron energy used. The fifth column shows the time taken for each run. The sixth column shows the net monitor counts as given by the RARAF facility for each run. The seventh column gives the fluence estimate for each run as supplied by Steve Marino at RARAF. Note, that for 1 MeV, they do not yet have a fluence estimate. This is because the 1 MeV runs were done in a configuration for which they did not have calibration data. In addition, there are a number of runs where monitor counting rates and hence neutron fluxes were not obtained. Finally, the last column lists other relevant information for particular runs.

Run Name	Azi. angle (deg.)	Polar angle (deg.)	Energy (MeV)	Time (s)	Net monitor count	n/cm^2	other
0304-144622	0	0	0.5	2100	764784	3.6E+05	HV=675; dist=81 cm
154410	0	0	0.84	2302	1011552	3.3E+05	
170803	0	0	1	1004.6	447359	-	
173347	-30	0	1	375.7	165522	-	
174743	-60	0	1	353.1	155316	-	
184332	+30	0	1	400	175743	-	
193247	0	0	1.5	1326	151381	2.2E+05	dist=58.8 cm
200904	0	0	2.0	1830	317884	3.9E+05	
210209	0	0	2.5	1561	308365	3.3E+05	
213948	0	0	Cf-252				
0305-104230	0	0	1.5	419.6	56918	8.2E+04	
110108	+28	0	1.5	640	112268	1.6E+05	
111632	-30	0	1.5	692.7	121118	1.7E+05	
113228	-60	0	1.5	624.2	107888	1.6E+05	
114942	-90	0	1.5	580.0	103006	1.5E+05	
121031	0	-30	1.5	585.4	107866	1.6E+05	
122856	0	-60	1.5	727.2	134902	1.9E+05	
124522	0	+30	1.5	575.0	102936	1.5E+05	
130548	0	0	1.5	690.8	124355	1.8E+05	
150500	0	0	5.8				
151856	0	0	5.8	2527.2	520889	5.2E+05	
160439	0	0	5.8				beam stop in; background
161114	0	0	5.8				HV=625
162015	0	0	5.8	2000	449514	4.4E+05	
183209	0	0	14				prompt/delay thresh=29
184853	0	0	14				HV=529
185613	0	0	14	1945	1554770	5.4E+05	
193201	0	0	14				

Table 1: List of NS runs at the RARAF facility.

3.1.3 Initial RARAF Results: Behavior of NS for E = 1.5 MeV

Here some initial results from RARAF are given for a beam energy of 1.5 MeV. Figure 3 shows the prompt pulse at a beam energy of 1.5 MeV. The prompt pulse measures the neutron energy deposition in the plastic scintillator (BC454) due to multiple proton recoil collisions. As shown here, there is a well defined peak around channel 15 due to the neutrons at 1.5 MeV. Based on other data, we suspect that the tail at lower channels is due to neutrons scattered from the concrete walls of the target room, which then have have lower energies.

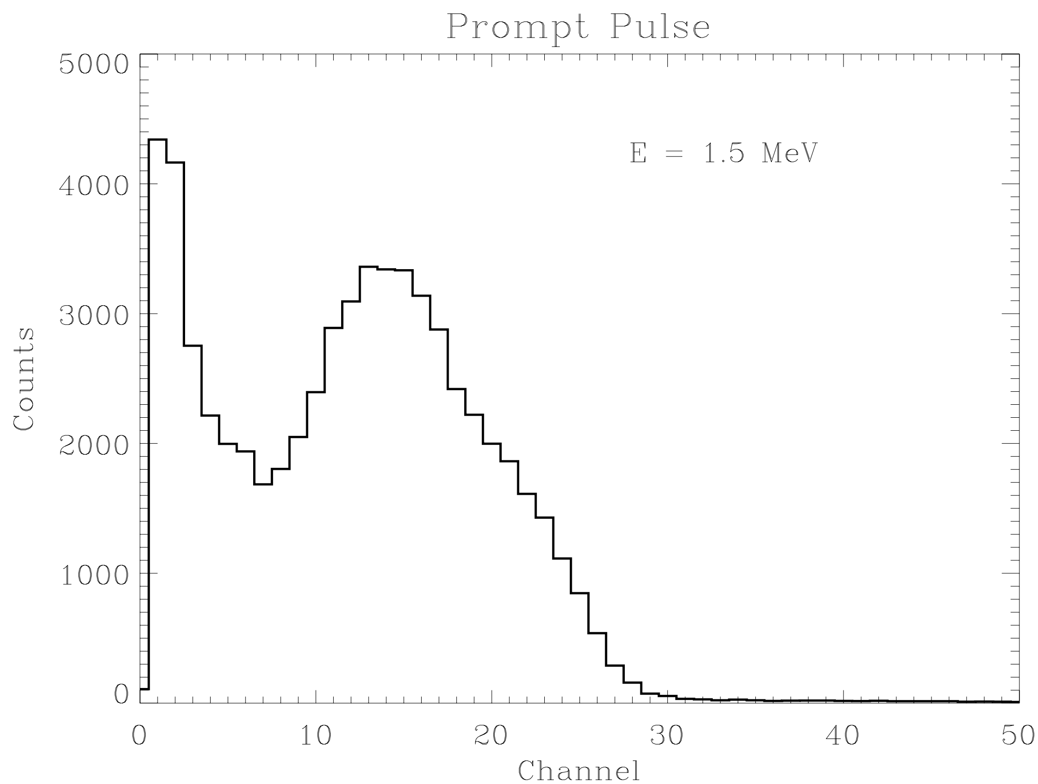

Figure 3: Prompt pulse for a neutron energy of 1.5 MeV

Figure 4 shows the delayed pulse for neutrons having an incident energy of 1.5 MeV. The peak around channel 50 is due to the $^{10}B(n,\alpha)^{7}Li^{*}$ reaction at an equivalent electron energy of 93 keV. The counts at high channels are due to the Compton continuum of 478 keV gamma-rays that are in coincidence with the charged-particle recoils.

Finally, Figure 5 shows a time-to-second pulse (TTSP) spectrum for neutrons of 1.5 MeV. The exponential portion at low channels is the expected spectrum for BC454 scintillator plastic. The flat portion at high channels is due to chance coincidences. After subtracting a background of 50 counts due to chance coincidences, the remaining spectrum (red curve) has an e-folding time of 1.98 μs, which is close to the expected time of 2 μs based on previous, finite sized BC454 sensors [*Feldman et al*., 1991, 1999].

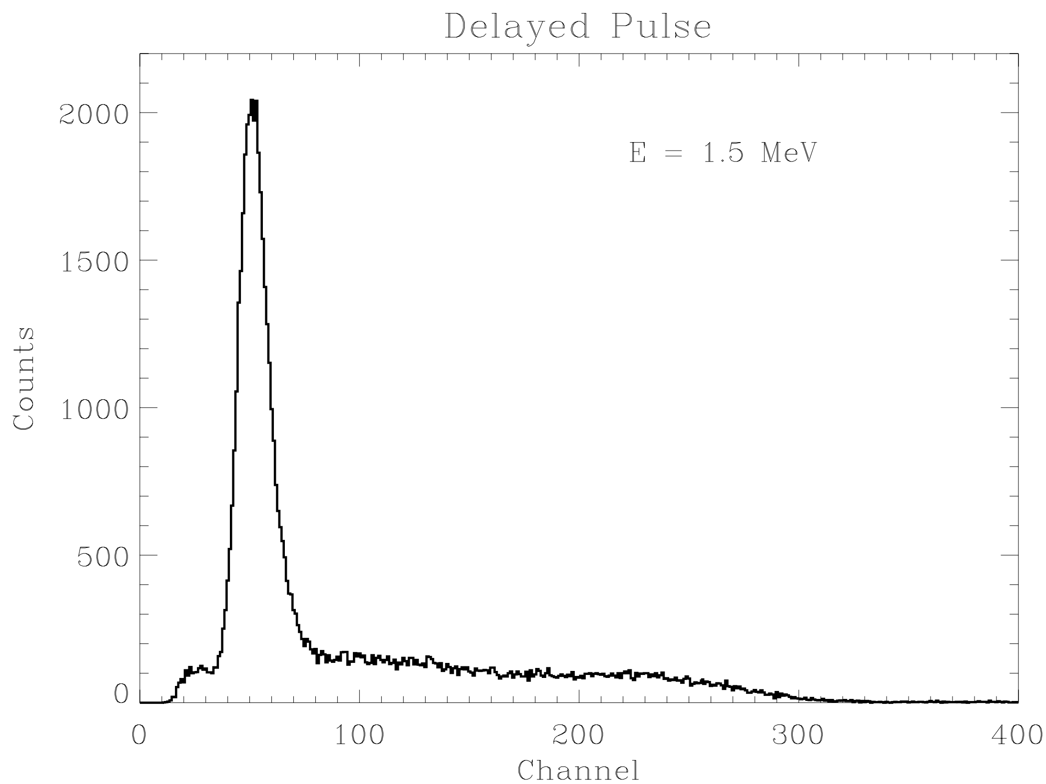

Figure 4: Delayed pulse for a neutron energy of 1.5 MeV

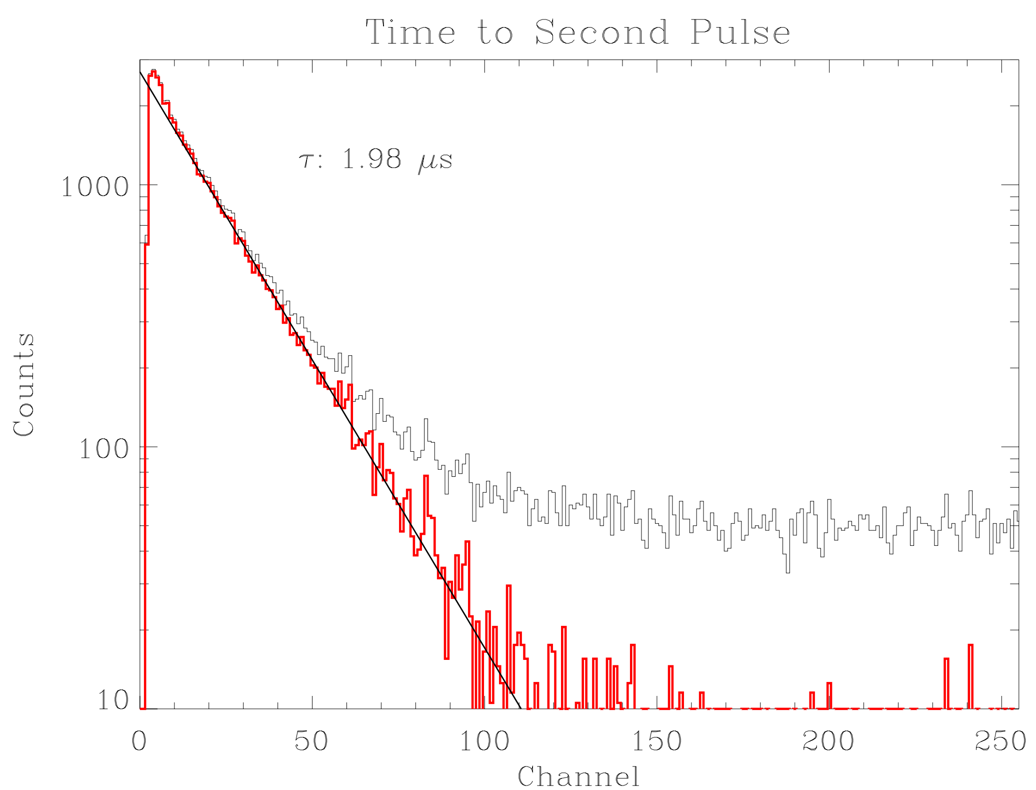

Figure 5: Time-to-second pulse signal for 1.5 MeV neutrons.

3.1.3 Initial RARAF Results: Behavior of NS for various energies

Figures 6 and 7 show data from all eight energies ranging from 0.5 to 14 MeV. Figure 6a shows data for the prompt pulse where the measured counts are plotted versus energy (see Figure 7 for how the energy scale is derived). Note that the counts for each energy in Figure 6a have been arbitrarily scaled to show all the data on one plot. This plot, therefore, cannot be used to get the absolute efficiency. In addition, for the highest two energies (5.8 and 14 MeV), the high voltage on the BC454 PMT needed to be lowered to keep the prompt pulse on scale (see Table 1 for the HV values). This gain change is reflected in Figure 6b where the peak positions of the delayed pulse are shifted to lower channels for 5.8 and 14 MeV.

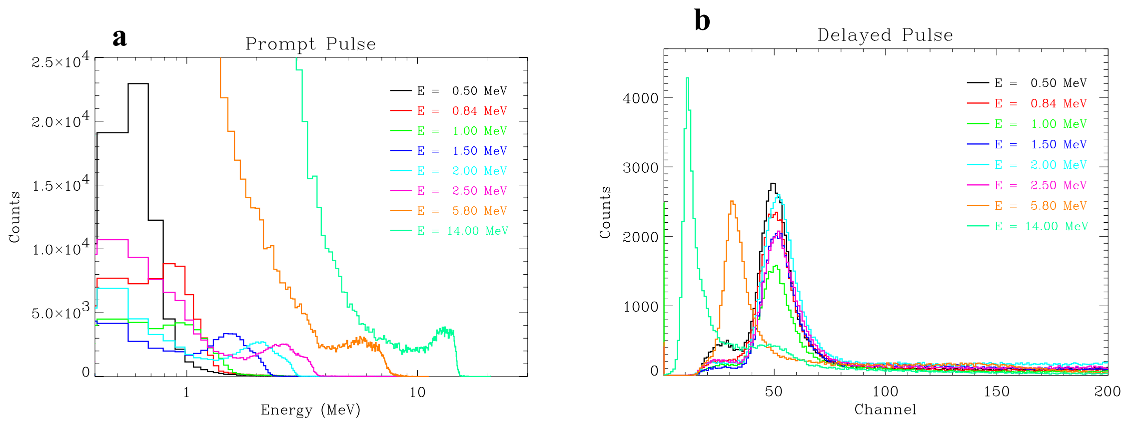

Figure 6: Prompt (a) and delayed (b) pulses for eight different neutron energies ranging from 0.5 to 14 MeV.

Figure 7 shows an energy calibration using prompt pulse data where the neutron energy is plotted versus gain-corrected channel number for the centroid of the prompt peak. Since the data points lie on a straight line in log/log space, a power law has been fit to the data (black line in Figure 7):

$$C = 6.7E^{1.69}, \quad (1)$$

where C is the channel number and E is the neutron energy. The power law exponent of 1.69 compares very favorably to the exponent of 1.6 that was determined by *Byrd and Urban,* [1994] for BC454 using a model of BC454 plastic (red line in Figure 7).

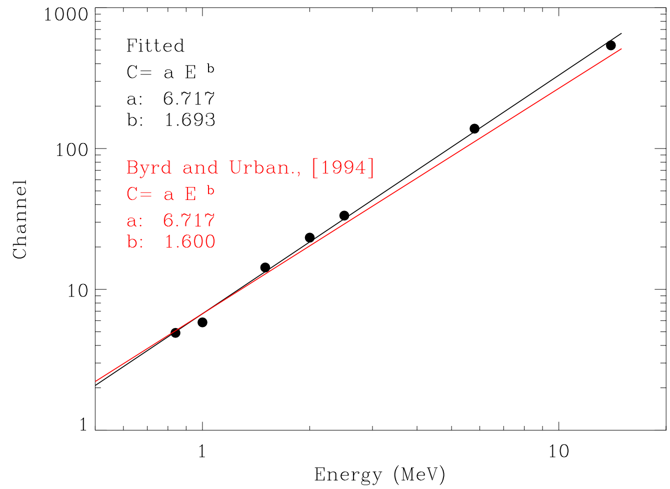

Figure 7: Plot of neutron energy versus the pulse height channel centroid for seven different neutron energies.

3.1.4 Further Analysis

Further work will be done on this data set. First, we will make estimates of absolute efficiency for the eight different energies measured at RARAF. However, such an estimate is likely to be complicated by the significant room background observed in these measurements. Therefore, a reasonable estimate of the efficiency may require that both the NS and surrounding RARAF facility be modeled to account for all the neutrons being measured. Second, we will investigate the angular dependence of the fast neutron measurements made at RARAF. This information will also benefit from a complete NS/RARAF model.

3.2 Thermal and Epithermal Neutron Calibrations

3.2.1 Set up of runs

Calibration data for thermal and epithermal neutrons were measured at the Free-air Neutron Source Facility at Los Alamos National Laboratory (LANL). The testing room, illustrated in Figure 8, was specifically designed to reduce interference from radiation returning from the walls, floor, and ceiling. Tests are done on a platform ~12 feet above the concrete floor. An elevator is used to raise equipment to the platform level. A neutron transport model of the room exists to determine backgrounds for various detector geometries. Figure 9 shows the instrument set up used for the tests. The orientation is the same as the RARAF tests in regards to the azimuthally angles. The neutron source was a ^{252}Cf source having total neutron production rate of 6.504 x 10^7 n/s. The energy spectrum for the ^{252}Cf source is given by *Lorch* [1973]:

$$N(E) = QEe^{-E/E_o} / E_o \quad (2)$$

where Q = 6.504 x 10^7 and E_o = 1.3 MeV. This flux is seen in Figure 10.

The sensor was placed 250 cm away from the source. The source was surrounded by a 22 cm diameter sphere of D_2O in order to moderate the higher energy ^{252}Cf neutrons to epithermal and thermal energies. In addition, the D_2O sphere was covered with Cd to cut off thermal neutrons. Therefore, epithermal neutrons are measured with the Cd on the

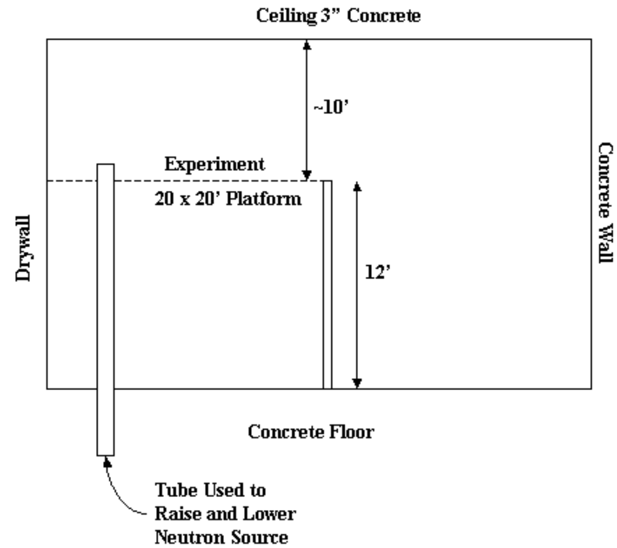

Figure 8. Schematic diagram of the "free-air source" neutron facility at LANL.

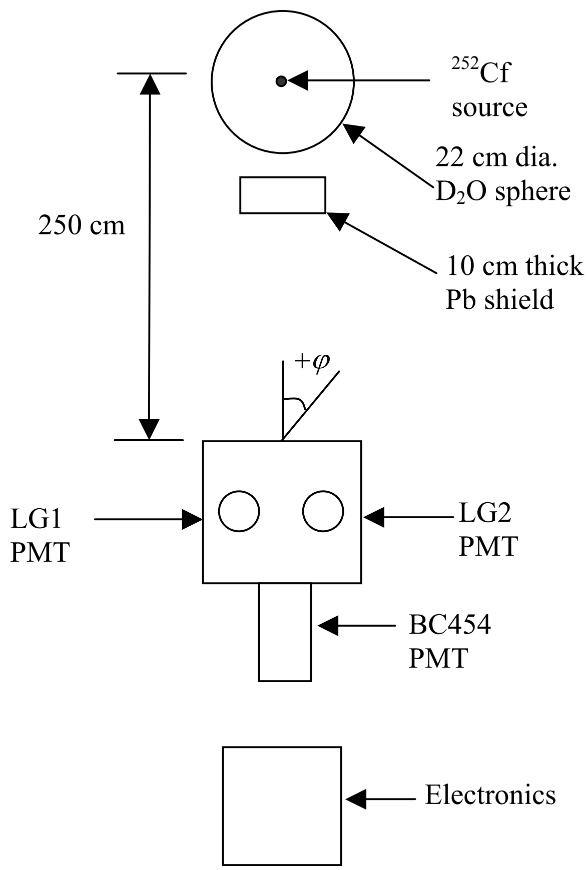

Figure 9. Schematic diagram of the NS set up at the LANL free-air facility.

D_2O sphere and thermal plus epithermal neutrons are measured when the Cd layer is removed from the D_2O sphere. Thermal neutrons are measured by taking the difference between the measured counts of the Cd and no Cd. Figure 11 shows a modeled ^{252}Cf neutron spectrum after it has been moderated through the D_2O sphere using MCNPX [*Waters*, 2002]. The power law shape of the moderated spectrum is very similar to the spectra that comes from the Moon or Mercury. However, this spectrum has a power law index of 0.88, while a lunar or Mercury spectrum has a power law index of 0.92 – 0.94.

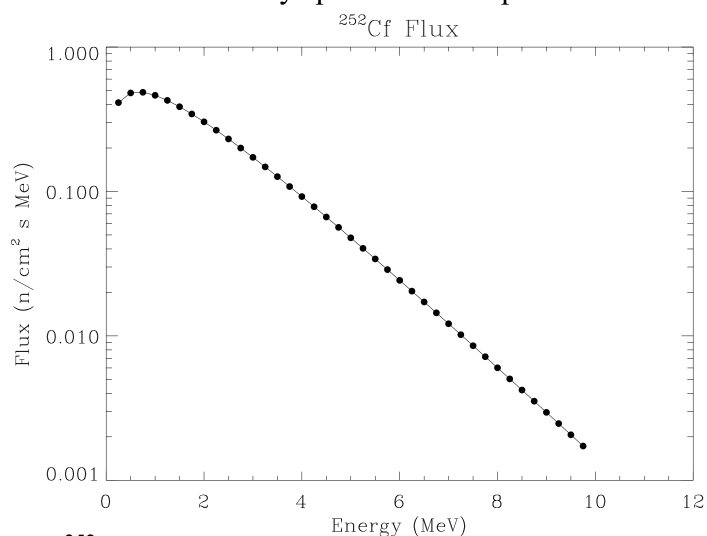

Figure 10: ^{252}Cf neutron energy spectra from *Lorch* [1973].

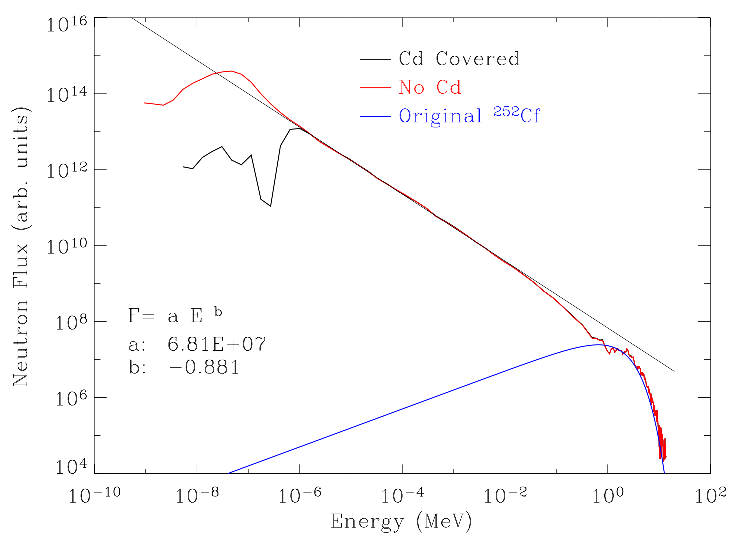

Figure 11: Modeled neutron flux spectrum for a ^{252}Cf flux spectrum (blue line) that has been moderated through a 22 cm diameter sphere of D_2O. The black line is when Cd covers the D_2O, the red line is for no Cd, and the straight line is a power law fit to the moderated spectra.

3.2.2 List of Runs

Table 2 lists the different runs that were carried out at LANL. The first column lists the run name, which is given by a date and time stamp. The second column shows either the azimuthally or polar angles given in degrees. The third column lists if Cd covers (or not covers) the D_2O sphere. Finally, the last column lists other relevant information for particular runs. Note that one run, 0408-163300, was carried out with the bare ^{252}Cf source and ran overnight in order to get good statistics on a full ^{252}Cf spectrum (see Section 4.1.4).

Run Name	Angle (deg)	Type	Comments
0408-102823	0 (azimuth)	Cd	
104950	+90	Cd	
110844	-90	Cd	
112653	-60	Cd	
114613	-30	Cd	
120350	+30	Cd	
122136	+60	Cd	
124705	0	No Cd	
130707	+90	No Cd	
132540	-90	No Cd	
134453	-60	No Cd	
140310	-30	No Cd	
142226	+30	No Cd	
143923	+60	No Cd	
145756	+15	No Cd	
151555	-15	No Cd	
154621	0	No Cd	shadow shield
163300	0	-	No D_2O; bare ^{252}Cf
0409-075245	0	Cd	shadow shield
082903	+15	Cd	No shadow shield
084727	-15	Cd	
114518	+45 (polar)	Cd	
120451	+30	Cd	
122821	+15	Cd	
124554	0	Cd	
130704	0	No Cd	
132557	+15	No Cd	
134422	+30	No Cd	
140246	+45	No Cd	
142830	0	No Cd	
150502	0	No Cd	

Table 2: List of NS runs at the LANL Free-air facility.

3.2.3 Initial Results from the LG sensors

Figure 12 shows initial results from the LG sensors. In particular, Figure 12 shows histograms of LG sensor data when each LG sensor was pointed directly toward the ^{252}Cf source. The black lines show thermal plus epithermal neutrons (i.e., no Cd on the D_2O sphere) and the red lines show epithermal neutrons (i.e., Cd was on the D_2O sphere). Very clear peaks are seen for both sensors. However, Figure 12b shows that for the higher counting rate thermal plus epithermal neutron data, the peak position is shifted to higher channels. It turns out that this is a general effect for the LG2 sensor as seen in Figure 13.

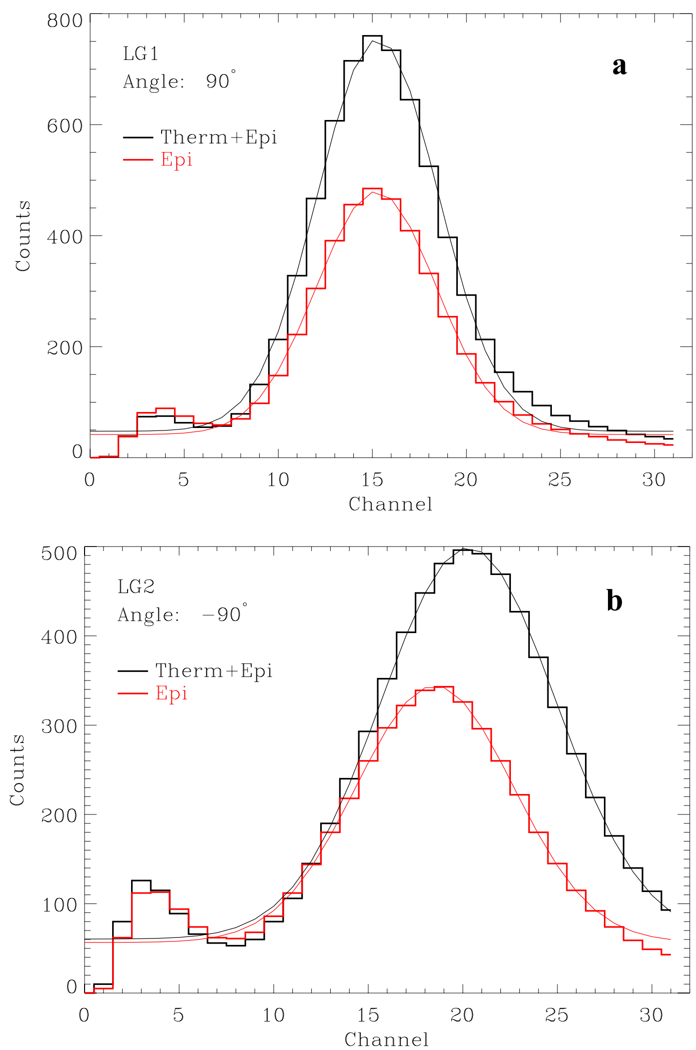

Figure 12: Histograms of LG sensor data when the NS is orientated at $\varphi = +90°$ for LG1 (a) and (b) $\varphi = -90°$ for LG2. The black lines show data when there was no Cd cover on the D_2O sphere, and the red lines show data when there was a Cd cover on the D_2O sphere.

In particular, Figure 13 shows that for the LG2 sensor, the peak position shifts to higher channels for higher counting rates. This effect is seen regardless of whether there is Cd on the D_2O sphere or not. In contrast, there is no peak shift for the LG1 sensor. There is speculation that this effect is caused by a floating dynode on the LG2 PMT, and is expected to be stable. Even with this effect, we do not expect a degradation in our ability to analyze the data as the total counting rate is the important measurement and not the peak position.

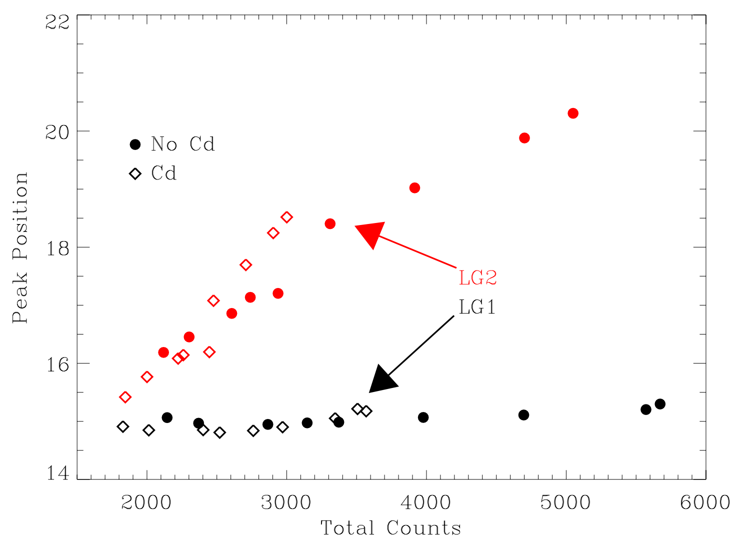

Figure 13: Plot of LG peak position as a function of total measured counts. LG1 data is given by black symbols; LG2 data is given by red symbols. Filled symbols show thermal plus epithermal neutrons; open symbols show epithermal neutrons.

Finally, Figure 14 shows a plot of LG counting rates as a function of azimuth angle. Since these are uncollimated, planar detectors, we expect that their angular response would have a $\cos\varphi$ dependence:

$$C = a\cos\varphi + b \quad (3)$$

Figure 12 shows that for both the LG1 and LG2 sensors, the angular dependence of the sensors when they are facing the source is well fit by a cos function with an offset. In order to properly understand the behavior of the sensors for greater angles, we need to carry out a detailed modeling of the NS sensor to account for the NS material and the background neutrons at the free-air facility. In summary, these data show that except for the counting rate dependence of the pulse height in LG1, the Li glass sensors work as expected.

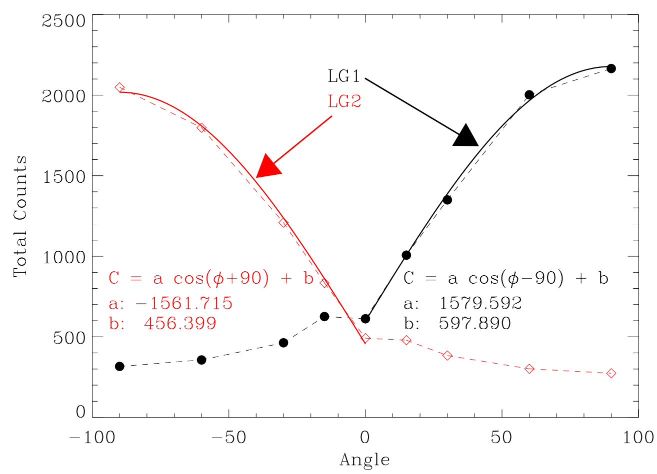

Figure 14: Total LG counting rate as a function of azimuth angle for the LG1 sensor (black symbols) and LG2 sensor (red symbols).

3.2.4 Fast neutron response for the extended ^{252}Cf run

One data collection run that deserves special attention is an extended run of the NS sensor in front of the bare ^{252}Cf source at the LANL Free-air facility. This run was started at the end of the first day of calibration and continued overnight until the next day for a total of 51,204 seconds. Because the energy spectra of ^{252}Cf extends to high energies of 10 MeV or higher, using ^{252}Cf is a good way to study the energy response of the BC454 plastic scintillator. Figure 15 shows BC454 data from the ^{252}Cf run. Figure 15a shows the prompt pulse, Figure 15b shows the delayed pulse, and Figure 15c shows the time-to-second pulse. All figures show the expected response. The prompt pulse, which indicates the neutron energy deposition in the scintillator, drops off for higher energies. This is due to both a decreasing neutron flux and neutron efficiency. Note, that the prompt pulse is plotted as a function of neutron energy using the energy scale determined in Section 3.1.3. The delayed pulse shows a very clear peak for the 478 keV gamma-ray as well as a Compton edge at higher energies. Finally, the time-to-second pulse shows the expected behavior of a ~2 μs e-folding time.

While these data are diagnostic as shown, they can also be used to determine absolute efficiency in a manner that is similar to what was done with the Lunar Prospector fast neutron detector [*Feldman et al.*, 2004]. This will be described in the next section.

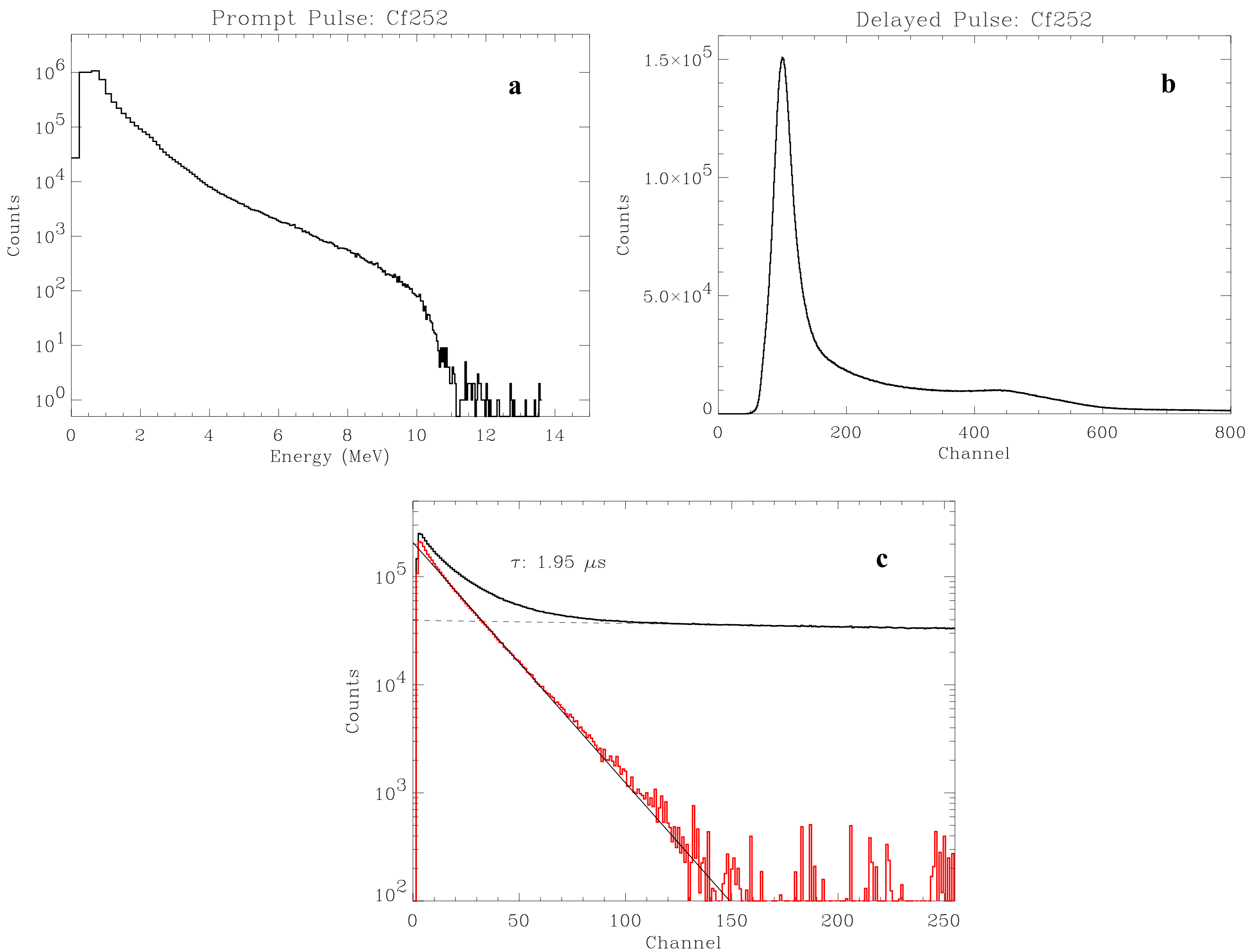

Figure 15: Prompt BC454 pulse (a), delayed BC454 pulse (b) and time-to-second pulse (c) for the extended 252Cf source run at the LANL Free-air facility.

3.2.4 Estimate the fast neutron efficiency with the bare ^{252}Cf source

In order to best estimate efficiency, we need to determine the true counting rate by subtracting off chance coincidences from the prompt and delayed pulses. This is done by taking early time pulses that are dominated by true neutron double pulses and subtracting the late time pulses that are dominated by chance coincidences using the following equation:

$$C_{true} = C_{early} - \frac{C_{late}}{\exp(-R\Delta t)}, \qquad (4)$$

where C_{early} are the early time counts (either prompt or delayed), C_{late} are the late time counts (either prompt or delayed), R is the singles counting rate in the BC454 plastic, and Δt is the time difference between early and late time counts. The exponent term in Equation 4 accounts for the Poisson probability that for higher counting rates, there is a larger accidental coincidence counting rate at early times than at late times. Here, we define early times as occurring between channels 4 and 54; late times are defined as between channels 200 and 250. Since each channel has a width of 0.1 µs, then the Δt in Equation 4 is 19.6 µs. The singles counting rate for the ^{252}Cf run was 9200 – 9400 cps, so that the exponential term has a value of 1.2.

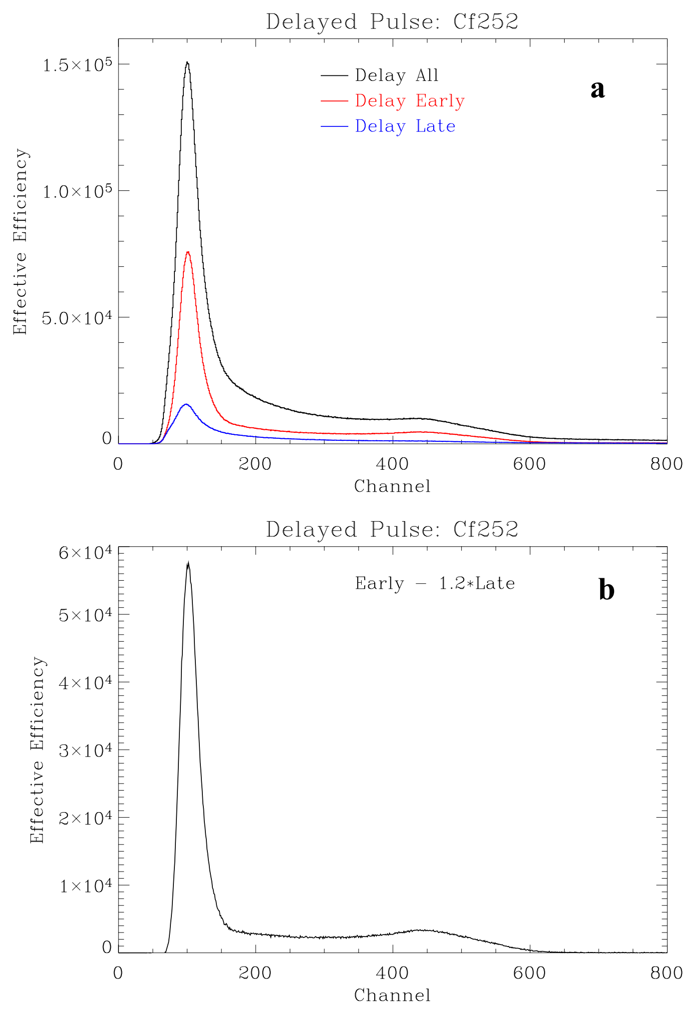

Figure 16: Delayed pulse as selected for early times and late times (a); corrected delayed pulse by subtracting 1.2 times the late time from the early time.

Figure 16 illustrates this correction with the delayed pulse. Figure 16a shows the original delayed pulse (black) and the delayed pulse as separated out by early times (red) and late times (blue). As seen, the early times have higher counting rates than late times. Figure

16b shows the corrected delayed pulse data using Equation 4. Here note that the counts at high channels go to zero while the counts in Figure 16a do not go to zero. This indicates that most of the accidental counts have now been removed from the delayed pulse data.

Now knowing how to determine the true neutron counting rate, we can make an expression of the measured prompt counting rate spectrum:

$$C(E) = \frac{F(E)\varepsilon(E)\Delta E A \Delta t}{4\pi R^2}. \quad (5)$$

Here, $C(E)$ is the corrected prompt counting rate, $F(E)$ is the ^{252}Cf neutron flux spectrum, $\varepsilon(E)$ is the BC454 efficiency, ΔE is the energy bin over which the counts were taken, A is the detector area, Δt is the time over which the counts were taken, and R is the distance from the sensor to the neutron source. First, we will define a counting rate that is independent of energy bin width, since the width changes as a function of energy (see Equation 1):

$$C'(E) = C(E) / \Delta E. \quad (6)$$

Second, we use Equation 2 for the functional form of the neutron energy spectrum. Third, based on the work of *Byrd and Urban* [1994] and also discussed by *Feldman et al*., [2004], the efficiency of the plastic scintillator can be expressed as follows:

$$\varepsilon(E) = k(E) / E \quad (7)$$

Putting all of this information together, Equation 5 becomes

$$C'(E) = \frac{NQ\exp(-E/E_o)}{E_o^2} k(E), \quad (8)$$

where,

$$N = \frac{A\Delta t}{4\pi R^2}. \quad (9)$$

The parameters of N have the following values: A = 100 cm^2; Δt = 51,204 b. b is a factor that accounts for the fact that only 255 events per second were collected during the ^{252}Cf run using event mode data and the total rate of double events was ~1200 events per second. The value of b is then b = 1200/255 = 4.7, which makes $\Delta t = 2.409 \times 10^5$ s. Finally, R = 250 cm. The value of N is then 30.7. The efficiency is therefore:

$$\varepsilon(E) = \frac{k(E)}{E} = \frac{C' E_o^2}{NQ\exp(-E/E_o)}. \quad (10)$$

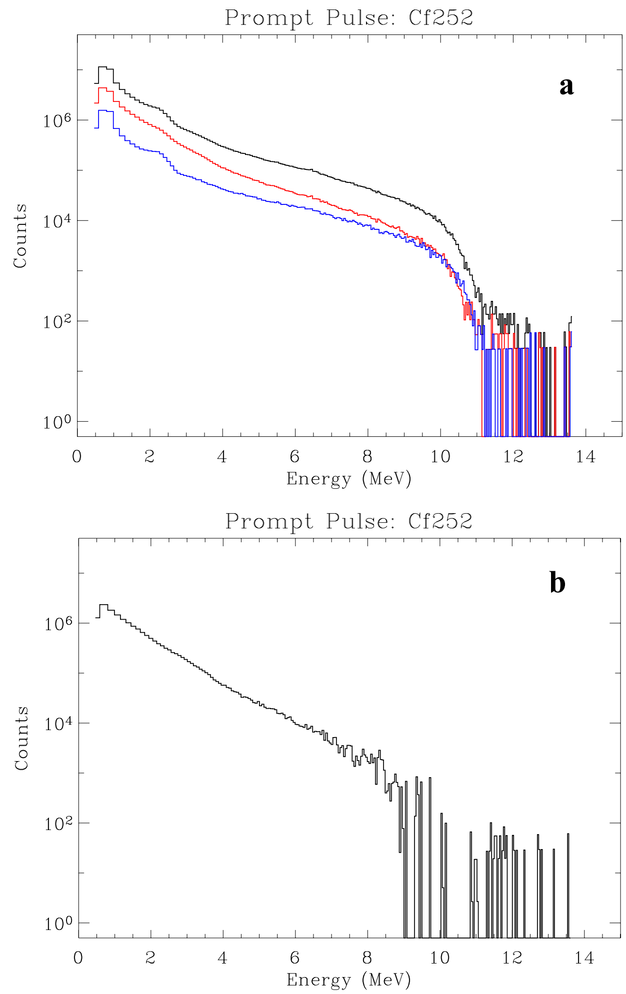

Figure 17: Figure 17a shows prompt pulse as selected for early times and late times (a). The black line is the original prompt data, the red line is early time, and the blue line is late time. Figure 17b shows corrected delayed pulse by subtracting 1.2 times the late time from the early time.

Figure 17 shows the prompt pulse data for early and late time (Figure 17a) and the early time corrected for late time (Figure 17b). These plots also show the counting rate after being corrected for the energy bin widths ΔE. In particular, the data in Figure 17b are the counting rate $C'(E)$ given by Equation 8. Figure 18 shows the calculated efficiencies as a function of energy as calculated by Equation 10. For 1 MeV, the efficiency is ~7%, which compares very favorably with the 8.2% calculated by *Byrd and Urban* [1994].

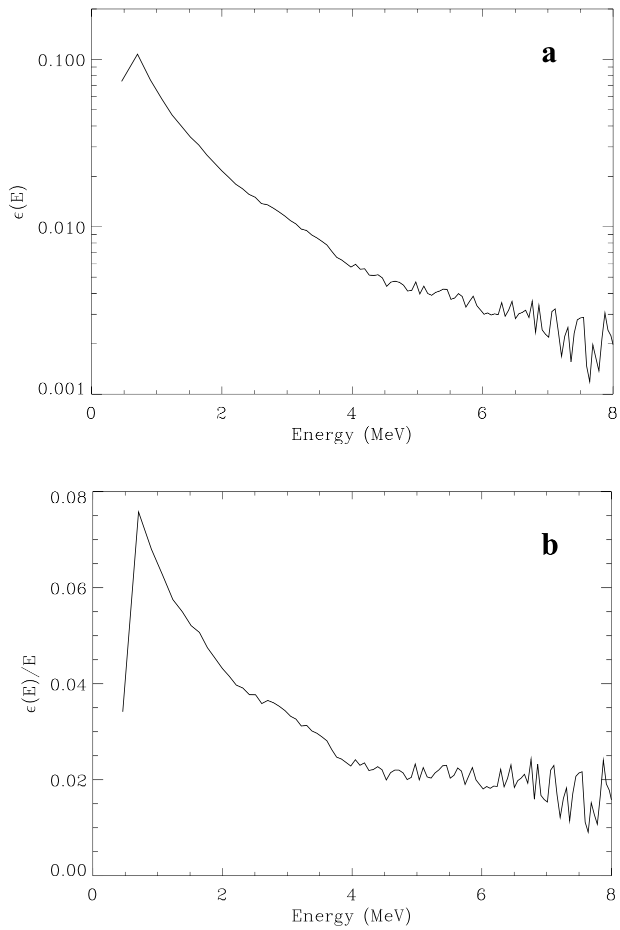

Figure 18: Calculated efficiencies as a function of energy. Figure 18a shows the efficiency $\varepsilon(E)$ and Figure 18b shows the efficiency scaled by energy E.

3.2.5 Further Work with the LANL data

Further work will be done in analyzing and interpreting these data. First, we plan to model the NS and the LANL facility. An MCNP model already exists for the LANL facility and it has been benchmarked with other projects. Therefore, we do not anticipate any difficulties in carrying out this work. The modeling work will enable us to estimate the NS efficiencies for the entire energy range of the instrument, including the Li glass efficiencies for thermal and epithermal neutrons. In addition, the model will help improve the estimate of fast neutron efficiency made in Section 3.2.4. Finally, the model will help confirm our understanding of the angular dependence of the Li glass and BC454 scintillators.

3.3 High Voltage and Gain Calibration measurements

High voltage and gain calibration measurement will be carried out on June 14 in Florida where the NS is currently installed on the spacecraft. These measurements will be done in a manner that is similar to what is described in the NS calibration plan.

4.0 Summary of Calibration Measurements

Aside from the desired high voltage and gain calibration measurements, we have completed all required calibration measurements for the Messenger NS. Based on the comparison of these measurements with models and other flight instruments, we conclude that the Messenger NS will meet or exceed all measurement requirements.

5.0 Data Products

The data runs are listed in Tables 1 and 2. The entire data will be delivered in a format agreed to by the instrument scientists and Messenger SOC. Additional data, such as modeling results, efficiencies, etc. will be provided as the work is completed.

References

Byrd, R.C., W.T. Urban, Calculations of the neutron response of boron-loaded scintillators, Los Alamos internal report, LA-12833-MS, 1994.

Feldman, W. C., G. F. Auchampaugh, and R. C. Byrd, A novel fast-neutron detector for space applications, *Nuc. Inst. and Methods Res. A*, A306, 350 – 365, 1991.

Feldman, W. C., B. L. Barraclough, K. R. Fuller, D. J. Lawrence, S. Maurice, M. C. Miller, T. H. Prettyman, and A. B. Binder, The Lunar Prospector Gamma-Ray and Neutron Spectrometers, *Nuc. Inst. and Methods Res. A*, 422, 562-566, 1999.

Feldman, W. C., K. Ahola, B. L. Barraclough, R. D. Belian, R. K. Black, R. C. Elphic, D. T. Everett, K. R. Fuller, J. Kroesche, D. J. Lawrence, S. L. Lawson, J. L. Longmire, S. Maurice, M. C. Miller, T. H. Prettyman, S. A. Storms, G.W. Thornton, The Gamma-Ray, Neutron, and Alpha-Particle Spectrometers for the Lunar Prospector Mission, *J. Geophys. Res. – Planets*, in press, 2004.

Lorch, E.A., Neutron spectra of 241Am/B, 241Am/Be, 241Am/F, 242Cm/Be, 238Pu/13C, and 252Cf isotopic neutron sources, *Int. Journal of Applied Rad. and Isotopes*, 24, 585 – 591, 1973.

Waters, L. S., MCNPX User's Manual, Version 2.3.0, Los Alamos National Laboratory report LAUR-02-2607, 2002.